THE JOURNAL OF BIOLOGICAL CHEMISTRY VOL. 290, NO. 2, pp. 1197–1209, January 9, 2015

Substrate-induced Changes in Domain Interaction of Vacuolar H^+-Pyrophosphatase*

Received for publication, March 26, 2014, and in revised form, November 19, 2014 Published, JBC Papers in Press, December 1, 2014, DOI 10.1074/jbc.M114.568139

Shen-Hsing Hsu[‡1], Yueh-Yu Lo[‡1], Tseng-Huang Liu[§], Yih-Jiuan Pan[§], Yun-Tzu Huang[§], Yuh-Ju Sun[§], Cheng-Chieh Hung[‡], Fan-Gang Tseng[¶], Chih-Wei Yang[‡2], and Rong-Long Pan[§3]

From the [‡]Department of Nephrology, Kidney Research Center, Chang Gung Memorial Hospital, Chang Gung University College of Medicine, Taoyuan 33333, the [§]Department of Life Science and Institute of Bioinformatics and Structural Biology, College of Life Science, and [¶]Department of Engineering and System Science, College of Nuclear Science, National Tsing Hua University, Hsin Chu 30013, Taiwan

Background: H^+-PPase is a PP_i-dependent proton translocase with 16 transmembrane domains embedded in a lipid bilayer.
Results: The domain interaction is observed by single molecule AFM, and the force peaks are changed in the presence of substrate.
Conclusion: The domains of PP_i-binding sites process the conformational change during substrate binding and hydrolysis.
Significance: This investigation provides significant mechanisms of the substrate binding and hydrolysis of H^+-PPase.

Single molecule atomic force microscopy (smAFM) was employed to unfold transmembrane domain interactions of a unique vacuolar H^+-pyrophosphatase (EC 3.6.1.1) from *Vigna radiata*. H^+-Pyrophosphatase is a membrane-embedded homodimeric protein containing a single type of polypeptide and links PP_i hydrolysis to proton translocation. Each subunit consists of 16 transmembrane domains with both ends facing the lumen side. In this investigation, H^+-pyrophosphatase was reconstituted into the lipid bilayer in the same orientation for efficient fishing out of the membrane by smAFM. The reconstituted H^+-pyrophosphatase in the lipid bilayer showed an authentically dimeric structure, and the size of each monomer was ~4 nm in length, ~2 nm in width, and ~1 nm in protrusion height. Upon extracting the H^+-pyrophosphatase out of the membrane, force-distance curves containing 10 peaks were obtained and assigned to distinct domains. In the presence of pyrophosphate, phosphate, and imidodiphosphate, the numbers of interaction curves were altered to 7, 8, and 10, respectively, concomitantly with significant modification in force strength. The substrate-binding residues were further replaced to verify these domain changes upon substrate binding. A working model is accordingly proposed to show the interactions between transmembrane domains of H^+-pyrophosphatase in the presence and absence of substrate and its analog.

Vacuolar H^+-pyrophosphatase (H^+-PPase[4]; EC 3.6.1.1) is a homodimeric membrane protein consisting of a single type of polypeptide with 14–17 transmembrane domains (TM) at a molecular mass of ~73 kDa on the vacuolar membrane (1, 2). The function of H^+-PPase is to generate proton gradients across endomembranes using the energy of the phosphoanhydride bond in pyrophosphate (PP_i) molecules, and therefore, this proton pump is considered as the fourth category of primary proton pumps (1, 2). H^+-PPase is mainly found in higher plants, some protozoa, eubacteria, and archaebacteria but not in animals. H^+-PPases are divided into two types as follows: K^+-dependent (type I) and K^+-independent (type II) H^+-PPases (3–5). Replacement of a conserved alanine residue at position 460 by a lysine converted the K^+-dependent into the K^+-independent form of H^+-PPase from *Carboxydothermus hydrogenoformans* (6), indicating that the Ala^{460} is involved in K^+ binding. Both H^+-PPase subfamilies required Mg^{2+} as the cofactor, whereas Ca^{2+}, Na^+, and F^- could inhibit the H^+-PPase activities to some extent (1, 6). The requirements and sensitivities of H^+-PPase to these ions might be attributed to the regulation of its enzymatic activities at the physiological level presumably through the conformational changes (7). In addition, radiation inactivation analysis revealed that the monomeric structure of H^+-PPase was adequate for PP_i hydrolysis, although homodimeric structure was necessary for proton translocation (8, 9). Furthermore, the dimeric structure of H^+-PPase was visualized by atomic force microscopy (AFM) and electron microscopy, respectively (10, 11). Previous studies showed the structure-function relationship of H^+-PPase and identified the pivotal domains and residues involved in enzymatic activities and structural integrity (1, 12–16).

* This work was supported by Chang Gung Memorial Hospital-National Tsing Hua University Joint Research Grants 101N2748E1 (to R.-L. P.) and CMRPG3D0641 (to C.-C. H.), National Science Council, Republic of China, Grants NSC 101-2627-M-007-008, NSC 102-2321-B-007-005, and NSC 102-2311-B-007-001-MY3 (to R.-L. P.), NSC 102-2314-B-182-031-MY3 (to C.-W. Y.), and NSC102-2811-B-182-028 (to Y.-Y. L.).
[1] Both authors contributed equally to this work.
[2] To whom correspondence may be addressed. Tel./Fax: 886-3-3281200-2506/03-3282173; E-mail: cwyang@ms1.hinet.net.
[3] To whom correspondence may be addressed. Tel./Fax: 886-3-5742688; E-mail: rlpan@life.nthu.edu.tw.

[4] The abbreviations used are: H^+-PPase, vacuolar H^+-pyrophosphatase; AFM, atomic force microscopy; F-D, force-distance curve; PP_i, pyrophosphate; smAFM, single molecule atomic force microscopy; SMFS, single-molecule force spectroscopy; TM, transmembrane domain; WLC, worm-like chain; aa, amino acid.

TABLE 1
Primers used in this study

	Forward (5′ → 3′)	Reverse (5′ → 3′)
C74S	CGTCGTCAAATCCGCCGAAATACAGAACG	CGTTCTGTATTTCGGCGGATTTGACGACG
C715S	CCAAAAGGGTCAGATTCCCACAAGGCAGC	GCTGCCTTGTGGGAATCTGACCCTTTTGG
C124S	CAAGCCCCCAGGCTTCCTCATACGATAAAAC	GTTTTATCGTATGAGGAAGCCTGGGGGCTTG
C132S	GATAAAACTAAAACGTCTAAGCCAGCACTTG	CAAGTGCTGGCTTAGACGTTTTAGTTTTATC
K250A	GGAGGTATTTATACCGCGGCTGCTGATGTTG	CAACATCAGCAGCCGCGGTATAAATACCTCC
K261A	GATCTCGTTGGCGCGGTTGAGAGAAACATTC	GAATGTTTCTCTCAACCGCGCCAACGAGATC
E268A	GAGAGAAACATTCCCGCAGATGATCCAAG	CTTGGATCATCTGCGGGAATGTTTCTCTC
D269A	GAAACATTCCCGAAGCTGATCCAAGAAATCC	GGATTTCTTGGATCAGCTTCGGGAATGTTTC
R441A	GTTGCTGACTCCTGCGCAACTGGTGCTGC	GCAGCACCAGTTGCGCAGGAGTCAGCAAC
R523A	GTCACAGAATTGCTGAGAGAACTGATGC	GCATCAGTTCTCTCAGCAATTCTGTGAC
D527A	CGTGAGAGAACTGCTGCCCTTGATGCTGC	GCAGCATCAAGGGCAGCAGTTCTCTCACG
E606A	CTCTGAAGATGGTTGCGGAAGTGCGCAGG	CCTGCGCACTTCCGCAACCATCTTCAGAG
K695A	GATAATGCAAAGGCGTACATTGAGGCTGG	CCAGCCTCAATGTACGCCTTTGCATTATC

Recently, the crystal structure of H^+-PPase from mung bean (*Vigna radiata* L.) has been solved, and the overall structure showed that the H^+-PPase is compactly folded in a rosette manner (2, 17). The rosette structure consists of two concentric walls with inner (TM5, -6, -11, -12, -15, and -16) and outer walls (TM1–4, -7–10, -13, and -14) (Fig. 1). The inner wall is responsible for substrate binding and the outer wall for the structural stability and integrity of this protein. Besides the transmembrane helix, the enzyme also contains two short helices (α2 and α3) on the cytosolic side and two additional helices (α1 and α4) together with two anti-parallel β-strands (β1 and β2) on the luminal side (2, 17). According to the x-ray crystal structure, several domains are suggested to participate in subunit interaction including TM5, -12, -15, and -16 on the inner wall and TM10 and -13 on the outer wall. The substrate/IDP-binding site is a funnel-shaped pocket formed by six core TMs, and this binding cage has an unusually acidic environment that contains 12 acidic residues, three lysine residues, and one asparagine residue. In the catalytic pocket, the substrate analogy IDP is surrounded by one K^+ and five Mg^{2+} that are involved in substrate binding. The three-dimensional structure of H^+-PPase elucidates probable mechanisms for substrate hydrolysis and proton translocation of this translocase; however, the process of domain association and the dynamic movements of H^+-PPase upon substrate binding and hydrolysis are still unclear. We were thus prompted to investigate the mechanism of dynamic changes between domains of vacuolar H^+-PPase.

AFM has been used as a powerful tool to examine the protein-protein interaction, especially of the transmembrane proteins (18–21). AFM-based single molecule force spectroscopy (SMFS) points and unfolds the domain-domain interaction networks directly for stabilizing the structure and for investigating the function of membrane proteins under lipid bilayer conditions (22). In SMFS, membrane proteins are unfolded stepwise at a steady pulling velocity to calculate the forces that are required to overcome energy barriers for maintaining structural segments of the protein. The sensitivity of interaction forces could be quantified to the range of piconewtons (pN), and the interaction region could be pinpointed precisely at nanometer or subnanometer resolution. Furthermore, the force-distance curves (F-Ds) measured by AFM would provide much more information on the domain-domain interaction of the proteins (23, 24). In this study, we employed the AFM F-Ds to analyze the H^+-PPase aligned in an artificial lipid bilayer to determine accordingly its domain-domain interaction force. The patterns of H^+-PPase F-Ds were modified upon substrate binding, which suggested domains of the active site might undergo dynamic movements to bind its substrate during PP_i hydrolysis.

EXPERIMENTAL PROCEDURES

Cloning, Expression, and Purification of His-tagged H^+-PPase—Cloning, expression, and purification of His-tagged H^+-PPase were performed as described previously with minor modifications (7). Mung bean (*V. radiata* L.) H^+-PPase cDNA (VPP; accession number P21616) was cloned into the *Escherichia coli*/*Saccharomyces cerevisiae* shuttle vector, pYES2 (Invitrogen), and the C terminus was fused with His_6 tag (pYVH6) for purification and reconstitution (7). The site-directed mutagenesis was carried out by the QuikChange™ method with the primers containing mutated oligonucleotides (Table 1) and then subcloned to the expression vector pYVH6 (13, 25). The mutated nucleotides were subsequently defined and confirmed by DNA sequencing. The pYVH6 and its relative variants were transformed into the yeast host cell *S. cerevisiae* strain BJ2168 (*MATa, prc-407, prb1-1122, pep4-3, leu2, trp1, ura3, GAL*) and cultured according to previous methods (7, 12, 13). The yeast microsomal membranes enriched in H^+-PPases were prepared followed by solubilization and purification with Ni^{2+}-nitrilotriacetic acid beads as described previously (7, 12, 13, 25).

Enzyme Assay and Protein Determination—PP_i hydrolysis activity was determined by measuring the release of P_i from PP_i as delineated previously (7, 12, 13, 26). The reaction medium contained 30 mM Tris/Mes (pH 8.0), 1 mM $MgSO_4$, 0.5 mM NaF, 50 mM KCl, 1 mM PP_i, 1.5 μg/ml gramicidin D, and 20–30 μg/ml microsomal protein. For assaying purified His-tagged protein, additional 0.1% (w/v) Triton X-100 and 80 μg/ml phosphatidylcholine (soybean, type IV-S, Sigma) were added to the reaction medium, and 5 μg of purified protein was included. The hydrolysis of pyrophosphate is linear with respect to the concentration of H^+-PPase that was up to 300 μg/ml and the reaction time to 10–20 min under this condition at 37 °C. After incubation, the reaction was terminated by a stop solution containing 1.7% (w/v) ammonium molybdate, 2% (w/v) SDS, and 0.02% (w/v) 1-amino-2-naphthol-4-sulfonic acid. The released P_i was determined by spectrophotometer as described elsewhere (16). The concentration of the protein was measured by

the dye-binding method of Bradford using BSA as standard (27).

Reconstitution of H^+-PPase into Lipid Bilayer—H^+-PPase reconstitution into artificial lipid bilayer was performed as reported previously with minor modifications (28). In brief, the preparation of liposome phosphocholine/1,2-dioleoyl-*sn*-glycero-3-phosphocholine was mixed at a ratio of 1:1 and dissolved in the chloroform/methanol (9:1) followed by overnight vacuum to remove the organic solvent. The dry lipids were rehydrated in phosphate-buffered saline (PBS) containing 0.1% (w/v) *n*-dodecyl β-D-maltoside to final concentration of 5 mg/ml. Following sonication in a bath-type sonicator for 5 min at 4 °C, the solution was freeze-thawed in liquid nitrogen for 10 cycles. Four micrograms of purified H^+-PPase in the buffer containing 20 mM HEPES (pH 7.2), 100 mM KCl, and 0.1% (w/v) *n*-dodecyl β-D-maltoside were mixed well with lipid and then injected into the Teflon wells. 1,2-Dioleoyl-*sn*-glycero-3-phosphocholine and 1,2-dioleoyl-*sn*-glycero-3-[(*N*-(5-amino-1-carboxypentyl)iminodiacetic acid) succinyl] (DOGS-NTA-Ni) were mixed at the ratio of 5:1, and the mixed lipid was dissolved in the chloroform/methanol (9:1) to a final concentration of 0.5 mg/ml. One μl of the mixed lipid was therefore added to the surface of the protein buffer on Teflon wells followed by gentle stirring for 1 h using stainless steel beads. The solution was then vacuumed for 20 min to eliminate organic solvent. The detergent was removed by adding 5 mg of Bio-Beads SM2 in the well for 5–6 h and a second addition for overnight incubation at 4 °C. The reconstituted H^+-PPase was sprayed on a freshly cleaved mica surface and then scanned with AFM.

AFM and SMFS Experiments—A commercial atomic force microscope (Nanoscope III; Digital Instruments, Santa Barbara, CA) with E type scanner and PicoForce module were used in this study (18, 19). The gold-coated silicon nitride (Si_3N_4) cantilevers (60 μm long) were utilized, and the nominal spring constant and resonance frequency were 30 pN/nm and 8 kHz in water, respectively. The spring constant of the individual AFM probe was determined in the buffer solution by the equipartition theorem prior to experiments (29). The H^+-PPase-enriched proteoliposomes were adsorbed onto freshly cleaved mica for 60–90 min at room temperature in adsorption buffer containing 20 mM Tris-HCl (pH 7.2), 150 mM KCl, and 50 mM $MgCl_2$. After adsorption, the mica surface was rinsed three times with adsorption buffer to remove weakly attached membranes. The substrate (PP_i), substrate analog (IDP), and product (P_i) were therefore added to final concentration of 20, 1, and 10 mM, respectively, for the following studies. Prior to SMFS, the region of membrane patch containing densely packed H^+-PPase was located by AFM imaging with contact mode. The force volume software takes a force curve from 999 points during a two-dimensional scan over H^+-PPase-enriched membrane patch. Force mapping images were measured over each 1×1-μm^2 regions.

F-D Analysis—Force mapping data were transformed to force extension curves for each subsection, and the area under the force extension curve was then calculated. The worm-like chain (WLC) fit of each force peak provided the contour length that reflected the amount of amino acids unfolded and stretched (24). The contour lengths and the corresponding rupture forces obtained were statistically analyzed using IgorPro 5 built-in and custom procedures (18, 19). The SPIP (Image Metrology ApS, Denmark) software was used for data analysis, and values of extraction force were thus determined with SigmaPlot software (SPSS, Chicago).

RESULTS

Characterization of Purified and Reconstituted H^+-PPases as a Dimer—The membrane topology predicts that H^+-PPase from *V. radiata* contains 16 transmembrane domains, and the crystal structure further indicates the 16 transmembrane α-helix structure as shown in Fig. 1 (2, 26, 30). H^+-PPase with His_6 tag at the C terminus was heterologously expressed in yeast and purified into a homogeneous form with high specific activity (7). The recombinant protein showed similar characteristics as those directly isolated from *V. radiata* (7). The purified and reconstituted state of H^+-PPase and its relative variants from heterologous expression on the yeast microsome were obtained and shown in SDS-PAGE and immunoblotting indicating a clear single band of highly purified protein for following studies (Fig. 2*A*). The molecular mass of yeast-expressed H^+-PPase is approximate 73 kDa (Fig. 2*A*). H^+-PPase was reconstituted into liposome using the dialysis and Bio-Beads absorption methods modified from previous works (10, 26, 28, 31, 32). This reconstitution method aligned all the H^+-PPase facing toward the same orientation with comparable specific activity to that on the yeast microsomal membrane (28, 33). Further properties of purified and reconstituted H^+-PPase were characterized as shown in Fig. 2*B*. For instance, K^+ stimulated the enzymatic activity of purified and reconstituted H^+-PPase by 4.5- and 3.9-fold, respectively. The sensitivities of reconstituted H^+-PPase to inhibitory ions, such as Na^+, F^-, and Ca^{2+}, were similar to those of purified H^+-PPase. The substrate analog imidodiphosphate (IDP) inhibited reconstituted H^+-PPase to a similar level as compared with its purified forms (Fig. 2*B*). It is conceivable that the properties of reconstituted H^+-PPase are functionally and structurally similar to its purified forms, verifying the feasibility of the following studies. The PP_i hydrolysis activities of H^+-PPase and its relevant variants, including C74S, C715S, C124S, C132S, K250A, K261A, E268A, D269A, R441A, R523A, D527A, E606A, and K695A variants, were measured, and some of these variants maintained about 80% PP_i hydrolysis activities except the K250A, K261A, E268A, D269A, R523A, D527A, E606A, and K695A variants to ~30% of the wild types, respectively (Fig. 2*C*).

The reconstituted H^+-PPase liposome was then sprayed on a freshly cleaved mica surface for AFM scanning (Fig. 3*A*) The AFM images showed that the membrane protein H^+-PPase was inserted into the lipid bilayer; the H^+-PPase-enriched liposome was then adsorbed on a mica surface (Fig. 3*B*). The membrane-embedded H^+-PPase with the cytosolic face protruded out the lipid bilayer for AFM probe scanning. For more detail on the structural information of reconstituted H^+-PPase, the scale of the AFM image was zoomed to 50×50 nm^2, and the results suggested that the H^+-PPase is aligned in dimeric structure with the size of each monomer of about 4 nm in length, 2 nm in width, and 1 nm in protrusion height (Fig. 3*C*). The volume of H^+-PPase measured by AFM is similar to that solved by x-ray

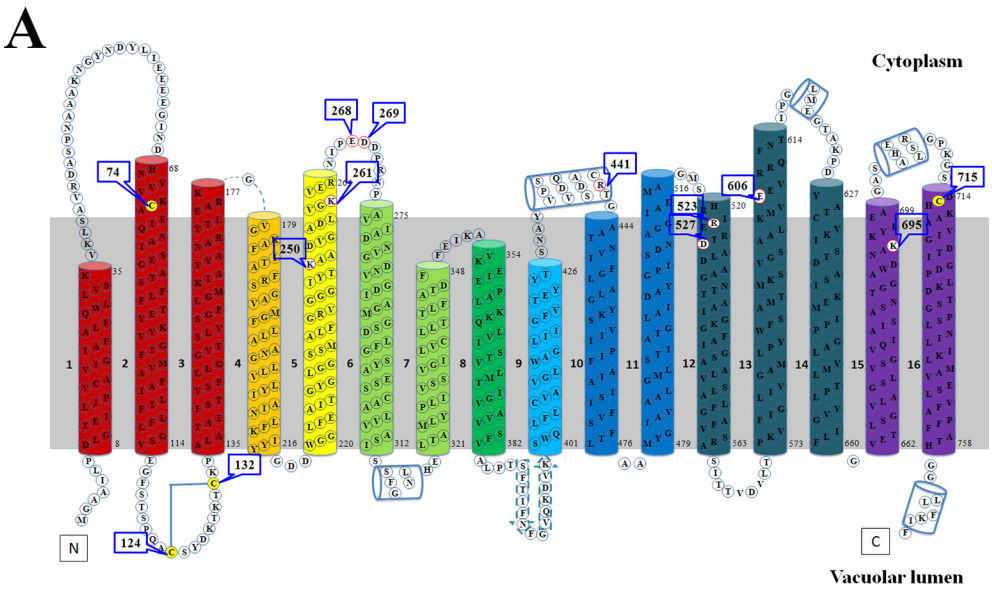
A
Cytoplasm
Vacuolar lumen
N
C
74
124
132
250
261
268
269
441
523
527
606
695
715
B
Cytosol
Lumen
C
NH2
COOH
NH2
COOH

crystal structure indicating that the AFM is a powerful tool for protein structure determination.

Identification of the H^+-PPase F-D and Its AFM Tip-binding Site—The AFM tip was used to extract the H^+-PPase polypeptide out of lipid bilayer (22). In Fig. 4*A*, the schematics show the procession of AFM probe pulling stepwise the H^+-PPase out of membrane. The liposome was used as mock (null membrane without H^+-PPase), and the results were smooth curves shown in Fig. 4*B, bottom panel*. When pulling either at the N- or C-terminal end of H^+-PPase, unfolded H^+-PPase could reach to maximal lengths of F-Ds. Therefore, we analyzed merely F-Ds that corresponded to the fully stretched length of H^+-PPase polypeptides unfolded from the lipid bilayer. Majority (more than 80%) of these F-Ds displayed 10 F-D peaks (Fig. 4*B, upper panel*). These 10 peaks obtained individually and sequentially were the force boundaries to maintain the H^+-PPase structure (Fig. 4, *B* and *C*). The stretched length and force strength of F-Ds were then fitted and calculated with worm-like chain (WLC) model (23, 34) as shown in Fig. 4*C*. To identify the attached site, the gold-coated AFM tip was used to form a gold-sulfur bond with cysteine residue either at loop 1 or loop 15 for the maximal length extractions of F-Ds. Because only two cysteine residues (Cys^{74} and Cys^{715}) were found along the C- and N-terminal region, it is conceivable that curves for a gold-coated AFM tip bound at these positions were primarily used to calculate the interaction forces. In addition, the Cys^{74} and Cys^{715} were further mutated to serine residues (C74S and C715S) for the F-D analysis to verify the AFM tip-binding sites (Fig. 4*D*). Within ~15,000 F-D analyses (the number of F-Ds is 3-fold more than WT), the C74S variant obviously showed no fully stretched F-Ds, whereas the C715S variant displayed a similar frequency of fully stretched F-Ds to the wild type H^+-PPase (Fig. 4*D*). Furthermore, the unfolding procedure was performed in the presence of 5 mM DTT to reduce the disulfide bond at Cys^{124}–Cys^{132} (Fig. 4*E*) (2). The force peak 1 was obviously rearranged in the presence of 5 mM DTT suggesting the original force barrier contributed by the disulfide bond was declined concomitantly with a decrease in the number of force peaks to 9 peaks (Fig. 4*E*). The Cys^{124} and Cys^{132} were further mutated to serine residues (C124S and C132S) for F-D analyses. The C124S and C132S variants generated the F-D curves with 9 peaks (Table 2), similar to DTT-treated H^+-PPase (Fig. 4*E*). These results demonstrated unambiguously that the Cys^{124}–Cys^{132} formed a disulfide bond and contributed to force peak 1 in F-D of wild type H^+-PPase. Taken together, the results showed that the gold-coated AFM tip anchored at the N-terminal loop of Cys^{74} forming the gold-sulfur bond at this position for the following measurements.

Notwithstanding, the 10 reproducible force peaks were further fitted using the WLC model to demonstrate the contour lengths of unfolded H^+-PPase polypeptide stretches. The length of the 10 force peaks occurred at the positions of 13 ± 2, 29 ± 3, 51 ± 3, 66 ± 4, 83 ± 3, 103 ± 2, 111 ± 4, 126 ± 4, 148 ± 4, and 174 ± 3 nm, respectively (Fig. 5*A* and Table 3). Because the AFM tip-binding site was located at Cys^{74}, the relative positions of these 10 force boundaries were therefore calculated at 121 ± 8, 177 ± 11, 259 ± 11, 312 ± 14, 375 ± 11, 446 ± 8, 475 ± 14, 527 ± 14, 607 ± 14, and 699 ± 11 amino acids (aa), respectively. These force boundaries were assigned at loop2 (113–129 aa), TM3–4 (166–188 aa), TM5-loop5 (248–270 aa), TM6–7 (298–326 aa), TM8 (364–386 aa), loop9-TM10 (432–454 aa), TM10–11 (461–489 aa), TM11–12 (513–541 aa), TM13-loop13 (593–621 aa), and TM15-loop15 (688–710 aa) according to the relative extraction length, respectively. The force strengths of these force boundaries were calculated as 91 ± 7, 102 ± 5, 131 ± 11, 163 ± 6, 181 ± 6, 174 ± 9, 176 ± 3, 203 ± 12, 154 ± 9, and 220 ± 7 pN, respectively (Fig. 5*A* and Table 3). To identify the force boundaries of H^+-PPase provoking these force peaks, the residues presumably for salt bridges such as Lys^{261}, Glu^{268}, Asp^{269}, Arg^{441}, Arg^{523}, Asp^{527}, and Glu^{606}, were changed to Ala residues, respectively. These variants were used for F-D analysis, and their force strengths are shown in Table 4. For example, interaction force of K261A, E268A, D269A, and R523A variants at force peak 3 were 84 ± 9, 92 ± 6, 87 ± 9, and 72 ± 9 pN, respectively (Table 4). In addition, force strength of R441A and E606A variants at force peak 6 were 92 ± 5 and 104 ± 7 pN, respectively. Moreover, the force strength of D527A and K695A variants were 103 ± 7 and 97 ± 6 pN, at force peaks 8 as well as 151 ± 11 and 114 ± 12 pN at force peaks 10, respectively. In sum, the force strength was reduced when replacing the relative salt bridge formation residues to Ala.

However, several F-Ds (~20% of total F-Ds) showed eight force peaks (Fig. 5*B*) and the relative positions of these eight boundaries were calculated accordingly at 123 ± 10, 175 ± 12, 259 ± 12, 315 ± 8, 374 ± 12, 445 ± 11, 478 ± 9, 704 ± 10 aa, respectively (Fig. 5*B* and Table 5). This set of force peaks lacking the force boundaries at force peaks 8 (TM11–12) and 9 (TM13-loop13) as compared with the 10 force boundaries mentioned above indicated that the two forces were presumably responsible for subunit interaction of the dimeric H^+-PPase (2). The relative positions of the 8 forces showed similar locations in comparison with the force peaks extracted from dimeric H^+-PPase (Fig. 5*A* and Table 3). Therefore, the remaining subunit embedded in the lipid bilayer was extracted by AFM tip lacking the two force boundaries.

F-Ds of H^+-PPase in Substrate-hydrolyzing Cycle—The substrate binding pocket consisted of TM5, -6, -11, -12, -15, and -16 and forms the inner wall of H^+-PPase, and several residues contributed hydrogen bonds or salt bridges with the IDP molecule as shown in the crystal structure (2). The substrate-induced conformational changes of H^+-PPase were described previously (2, 7, 26), and the precise movements of the active

FIGURE 1. **Structure of H^+-PPase.** *A,* transmembrane topology of H^+-PPase. Membrane topology of H^+-PPase shows 16 transmembrane domains with catalytic loops facing the cytosolic side and N/C termini facing the vacuolar side. The colors of the transmembrane domains indicated the force boundaries of H^+-PPase extracted by AFM probe, and Cys^{74} indicated the gold-coated AFM probe-binding site. *B,* crystal structure of the *Vr*H^+-PPase. H^+-PPase is a dimeric membrane-embedded protein shown as a ribbon diagram with height and width dimensions of 75 and 85 Å, respectively. The *dashed lines* in loop 1 indicate the missing information in the x-ray structure. The different colors of transmembrane domains indicated the force boundaries of H^+-PPase as determined by AFM. *C,* transmembrane domain distribution of H^+-PPase. The cytosolic view of the dimeric H^+-PPase showed the neighboring helices between transmembrane domains or the two subunits.

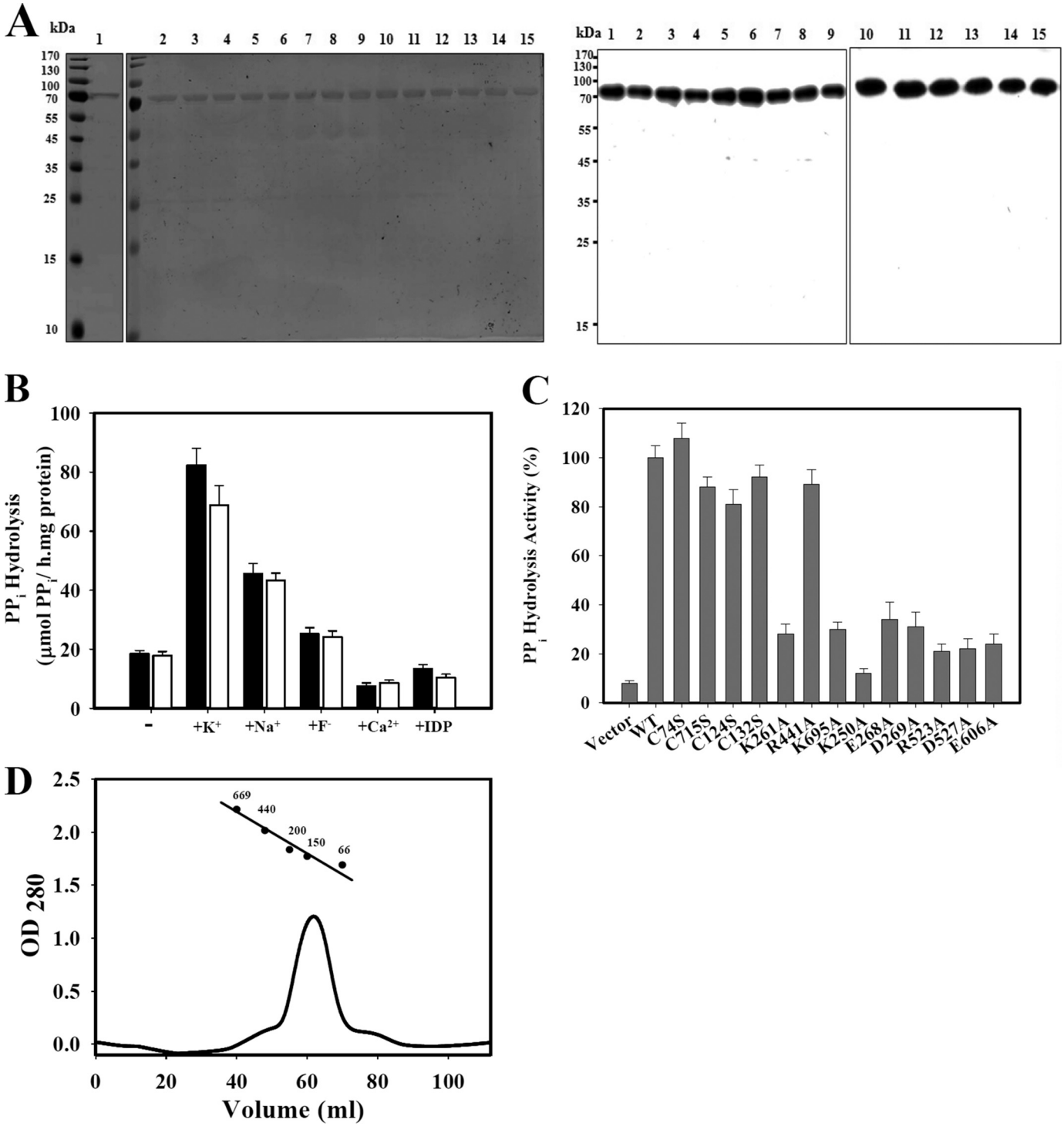

FIGURE 2. **Characterization of the purified and reconstituted H^+-PPase.** *A,* SDS-PAGE and Western blot of purified and reconstituted H^+-PPase variants. *Left panel,* SDS-PAGE; *right panel,* Western blot. The molecular mass of H^+-PPase is about 73 kDa. *Lane 1,* purified H^+-PPase; *lane 2,* reconstituted H^+-PPase; *lanes 3–15,* reconstituted C74S, C715S, C124S, C132S, K261A, R441A, K695A, K250A, E268A, D269A, R523A, D527A, and E606A variants, respectively. Molecular mass (kDa) markers are indicated on the *left*. *B,* activity assays of purified and reconstituted H^+-PPases. The specific activities of purified (*black*) and reconstituted (*white*) H^+-PPases were assayed in the presence of ions such as K^+, Na^+, F^-, and Ca^{2+}, and the substrate analog IDP, at concentrations of 50, 100, 20, 0.1, and 5 mM, if any. *C,* activity assays of reconstituted H^+-PPase variants. *D,* size exclusion chromatography of purified H^+-PPase. The molecular mass of purified H^+-PPase was determined by using a Superdex 200-pg 16/60 column, and the standard markers were thyroglobulin (669 kDa), ferritin (440 kDa), alcohol dehydrogenase (200 kDa), γ-globulin (150 kDa), and albumin (66 kDa).

site were further identified by AFM F-Ds. In the presence of substrate PP_i, the substrate was bound and hydrolyzed by H^+-PPase in the catalytic cycle (2, 17). During PP_i hydrolysis and proton translocation, the substrates bind to the inner wall of H^+-PPase developing the catalytic conformation for enzymatic activity. The substrates could be hydrolyzed during the F-D process, and a relatively high concentration of PP_i could also inhibit the enzymatic activity (1). Therefore, 20 mM PP_i was

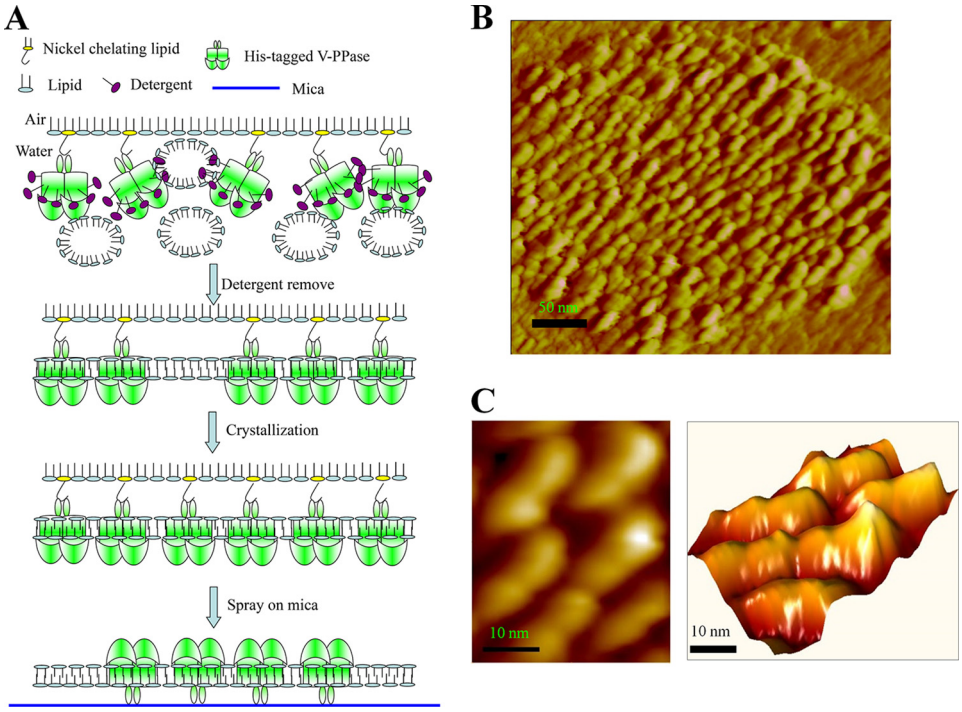

FIGURE 3. **Reconstitution of H$^+$-PPase into lipid bilayer.** *A,* schematics revealing reconstitution procedures of H$^+$-PPase onto liposomal membrane. Purified H$^+$-PPase was reconstituted into artificial lipid in the same orientation using the method described under "Experimental Procedures." *B,* AFM image of reconstituted H$^+$-PPase into the lipid bilayer. The reconstituted H$^+$-PPase was transferred to freshly cleaved mica surface and then scanned by AFM. The lipid membrane was sprayed on the mica surface and H$^+$-PPase protein particle was embedded in the membrane as the dimeric structure observed by AFM. *C,* high resolution images of H$^+$-PPase dimeric structure. The size of each subunit is ~4 nm in length, ~2 nm in width, and ~1 nm in height, and the *left panel* is in two-dimensional view, and the *right panel* is in three-dimensional view.

used in the measurement of F-Ds of H$^+$-PPase to maintain the H$^+$-PPase·substrate complex during the F-D procedure. From the statistical analysis, the numbers of force peaks were reduced to 8 curves as compare with the control state (Fig. 5*C*). The positions of the 8 force peaks were at 126 ± 8, 181 ± 11, 283 ± 8, 416 ± 8, 481 ± 11, 558 ± 11, 609 ± 14, and 703 ± 14 aa, respectively. The force strength of these 8 force peaks were 94 ± 5, 104 ± 8, 199 ± 8, 197 ± 10, 193 ± 8, 200 ± 7, 221 ± 8, and 223 ± 12 pN, respectively (Table 3). The force peaks 3 and 4 were obviously rearranged, and the force boundary shifted to loop5-TM6. The force peak 5 was reduced indicating the PP_i binding lessened force boundaries (Fig. 5*C*). The substrate binding of H$^+$-PPase induced conformational changes of the active sites and the force boundaries rearrangements.

In the pulling of H$^+$-PPase out of membrane, 10 mM P_i was present in the chamber and the F-Ds were detected under the same condition. The number of H$^+$-PPase force peaks was consequently restored to 10, similar to those of the control state (Fig. 5*D*). The positions of the 10 force peaks were, however, at 125 ± 8, 181 ± 8, 257 ± 14, 314 ± 11, 376 ± 11, 447 ± 11, 476 ± 11, 553 ± 8, 602 ± 11, and 698 ± 11 aa, respectively (Table 3). The force strength of the 10 force peaks were accordingly calculated as 89 ± 9, 104 ± 5, 129 ± 10, 160 ± 8, 187 ± 9, 170 ± 9, 178 ± 8, 200 ± 11, 160 ± 8, and 222 ± 11 pN, respectively (Fig. 5*D* and Table 3).

F-Ds of H$^+$-PPase were altered as well in the presence of the substrate analog IDP as compared with control state (Fig. 5*E*). The numbers of force peaks were thus reduced to 7 curves (Fig. 5*E*). In the presence of IDP, the new rearrangement force boundary was shifted to 281 ± 14 aa, the position between force peaks 3 (259 ± 11 aa) and 4 (312 ± 14 aa) in control state with a concomitant increase in force strength to 223 ± 9 pN (Table 3). Nevertheless, the force peaks 5 and 6 were decreased to basal level (Fig. 5*E*). In the presence of IDP, the positions of force peaks 7–10 occurred at similar positions as compared with control state. In contrast, the force strength of force peaks 7–10 were correspondingly increased to 227 ± 11, 220 ± 10, 176 ± 9, and 239 ± 8 pN, respectively (Table 3). For further identification of F-Ds in the substrate-hydrolyzing cycle, the residues involved in substrate binding, including Lys^{250} and Lys^{695}, were substituted to Ala residue, and the F-Ds were measured (Table 4). The number of force peaks in these variants was similar to WT. In the presence of IDP, the number of WT H$^+$-PPase F-Ds were reduced to 7 as compared with the control state. The numbers of F-Ds in K261A, E268A, D269A, R441A, R523A, D527A, and E606A variants were the same as that of WT in the presence of IDP. However, the force peaks numbers of K250A and K695A variants were altered to 8 with the original force peaks 3 and 4 separated individually as compared with WT in the presence of IDP. This result provided additional evidence for the substrate-induced changes in the domain interaction of H$^+$-PPase. Furthermore, in the presence of PP_i, the peak numbers of K261A, E268A, D269A, R441A, R523A, D527A, and E606A variants were the same as that of WT, whereas in K250A and K695A variants, the peak numbers were restored to 9, respectively. However, in the presence of P_i, the peak numbers of K250A and K695A variants were restored to 10, similar to WT H$^+$-PPase in the presence of product, P_i (Table 4).

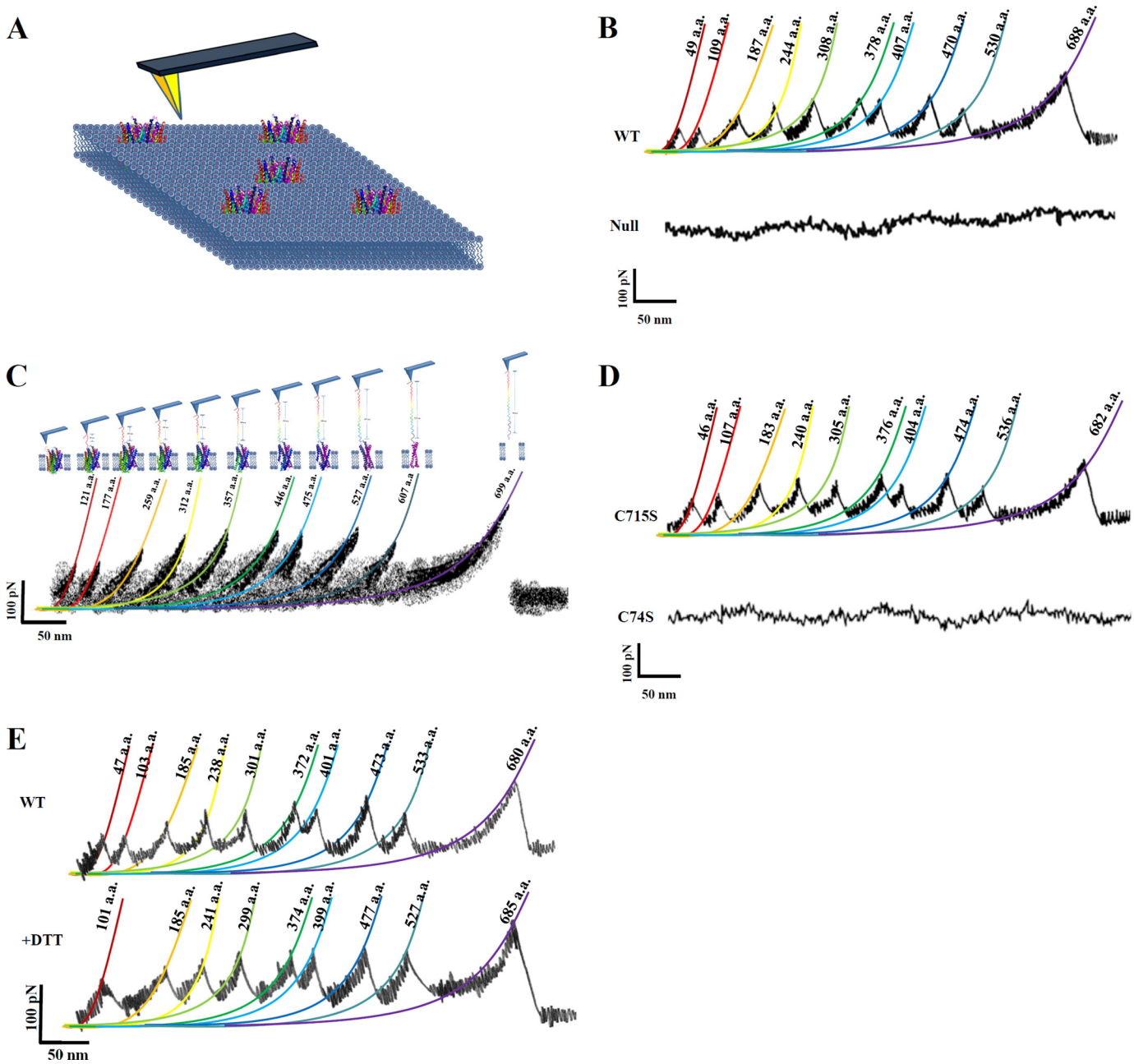

FIGURE 4. **Unfolding pathway of H^+-PPase.** *A,* extraction of H^+-PPase out of the membrane. The schematic indicates that the reconstituted H^+-PPase was embedded in a lipid bilayer, and the AFM probe was used to unfold H^+-PPase from the lipid bilayer. *B,* F-Ds of H^+-PPase (*upper panel*) and null membrane (*bottom panel*). The full length of the extraction curves was selected and analyzed to identify the force boundaries of H^+-PPase. *C,* superimposition of the F-Ds. Superimposition of F-D curves recorded during the unfolding of a single H^+-PPase. *Colored lines* are WLC fits of force peaks that reveal the contour length of the stretched polypeptide. The F-Ds were superimposed and analyzed for each force with their positions as marked. *D,* F-Ds of C74S and C715S variants. Variants with two residues (Cys^{74} and Cys^{715}) mutated were subjected to F-D analysis for identifying the AFM probe-binding site. *E,* effects of reducing agent on H^+-PPase F-Ds. The F-Ds of H^+-PPase were performed in the presence and absence of 5 mM DTT, respectively.

TABLE 2

The force strength of 10 force peaks under F-D analysis of different H^+-PPase variants relative to AFM tip-binding residues and disulfide-bound formation

The dash indicates those not detectable on the AFM F-Ds.

Strength (pN)	Force 1	Force 2	Force 3	Force 4	Force 5	Force 6	Force 7	Force 8	Force 9	Force 10
WT	91 ± 7	102 ± 5	131 ± 11	163 ± 6	181 ± 6	174 ± 9	176 ± 3	203 ± 12	154 ± 9	220 ± 7
C74S	–	–	–	–	–	–	–	–	–	–
C715S	88 ± 6	100 ± 9	134 ± 7	165 ± 3	183 ± 7	170 ± 5	174 ± 5	199 ± 11	159 ± 6	188 ± 9
C124S	–	108 ± 7	135 ± 6	159 ± 5	184 ± 11	171 ± 6	178 ± 11	191 ± 6	152 ± 3	201 ± 6
C132S	–	104 ± 5	128 ± 7	158 ± 11	177 ± 7	167 ± 6	170 ± 11	208 ± 6	150 ± 9	194 ± 11

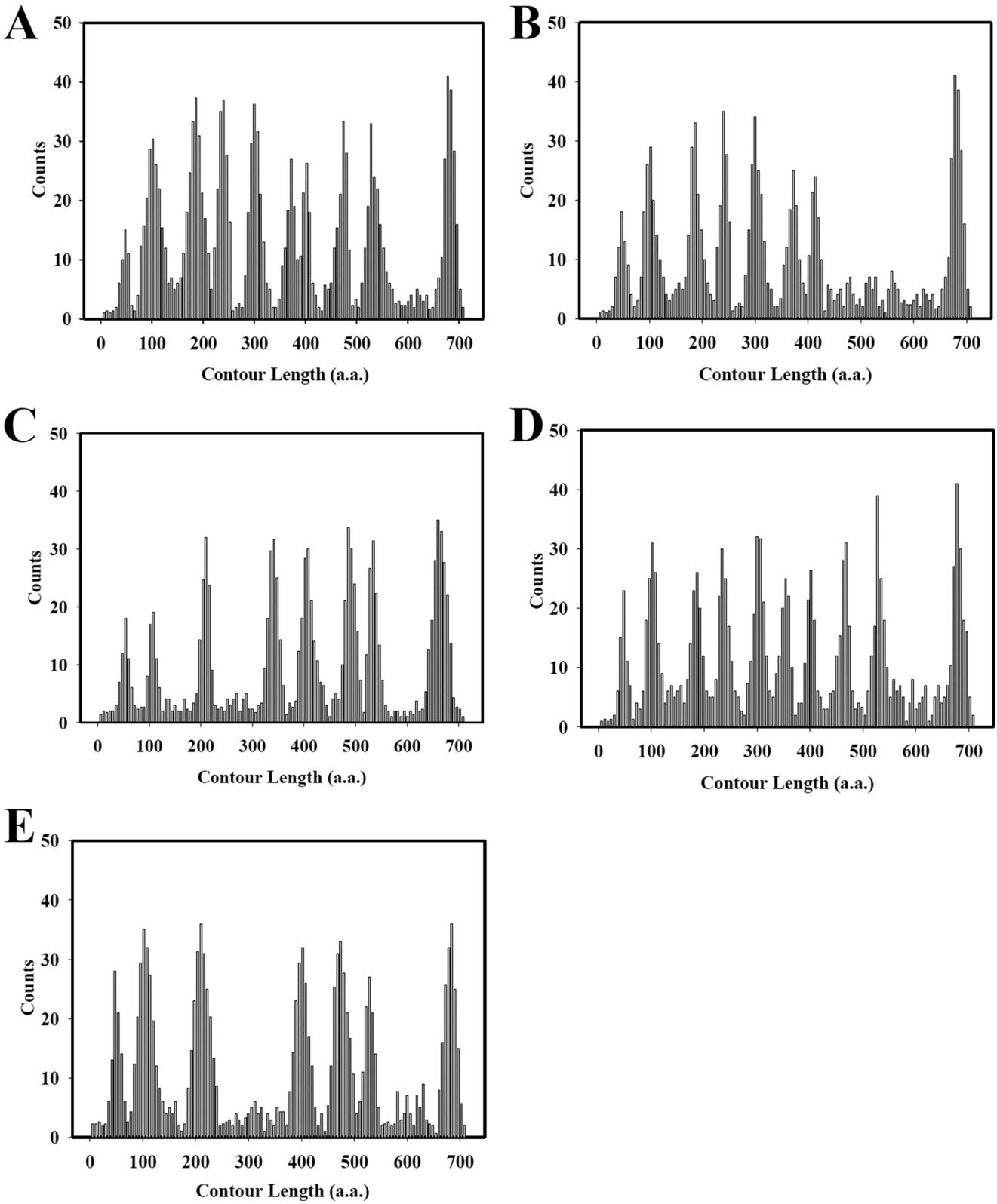

FIGURE 5. **Substrate-induced changes in transmembrane domain interaction of H^+-PPase.** Histograms showing the number of events at which contour lengths were fitted to the force peaks in F-D curves that recorded at different conditions. The F-Ds of H^+-PPase were analyzed under different conditions, including control condition, substrate PP_i, product P_i, and substrate analog (IDP). The force peaks were detected in the F-Ds, and the probability of force peaks generated was plotted *versus* the length of the stretched polypeptide. *A,* frequencies of 80% force peaks occur in substrate-free medium. *B,* frequencies of 20% force peaks occur in substrate-free medium. *C–E,* frequencies of force peaks occur in the presence of substrate PP_i, products P_i, and substrate analog IDP, respectively.

TABLE 3

Locations and force strength of the force boundaries

Count lengths represent most probable peak positions (calculated in amino acids) obtained from Gaussian fits to the count length distributions (Fig. 5). The dash indicates those not detectable on the AFM F-Ds.

	Force 1	Force 2	Force 3	Force 4	Force 5	Force 6	Force 7	Force 8	Force 9	Force 10
Control										
Length (aa)	121 ± 8	177 ± 11	259 ± 11	312 ± 14	375 ± 11	446 ± 8	475 ± 14	527 ± 14	607 ± 14	699 ± 11
Strength (pN)	91 ± 7	102 ± 5	131 ± 11	163 ± 6	181 ± 6	174 ± 9	176 ± 3	203 ± 12	154 ± 9	220 ± 7
PP_i										
Length (aa)	126 ± 8	181 ± 11	283 ± 8		–	416 ± 8	481 ± 11	558 ± 11	609 ± 14	703 ± 14
Strength (pN)	94 ± 5	104 ± 8	199 ± 8		–	197 ± 10	193 ± 8	200 ± 7	221 ± 8	223 ± 12
P_i										
Length (aa)	125 ± 8	181 ± 8	257 ± 14	314 ± 11	376 ± 11	447 ± 11	476 ± 11	553 ± 8	602 ± 11	698 ± 11
Strength (pN)	89 ± 9	104 ± 5	129 ± 10	160 ± 8	187 ± 9	170 ± 9	178 ± 8	200 ± 11	160 ± 8	222 ± 11
IDP										
Length (aa)	125 ± 8	177 ± 11	281 ± 14		–	–	472 ± 8	550 ± 14	602 ± 11	704 ± 14
Strength (pN)	101 ± 7	98 ± 5	223 ± 9		–	–	227 ± 11	220 ± 10	176 ± 9	239 ± 8

TABLE 4

The force strength of 10 force peaks under F-Ds analysis of different H^+-PPase variants in the presence of substrate, substrate analog, and product

The "–" indicates those not detectable on the AFM F-Ds.

Strength (pN)	Force 1	Force 2	Force 3	Force 4	Force 5	Force 6	Force 7	Force 8	Force 9	Force 10
Control										
K250A	90 ± 11	99 ± 9	133 ± 6	164 ± 9	179 ± 11	169 ± 6	178 ± 7	201 ± 7	151 ± 11	211 ± 9
K261A	94 ± 11	97 ± 6	84 ± 9	167 ± 6	180 ± 9	170 ± 7	180 ± 11	190 ± 5	161 ± 12	231 ± 11
E268A	95 ± 7	104 ± 5	92 ± 6	166 ± 5	178 ± 9	171 ± 3	177 ± 12	204 ± 9	156 ± 6	224 ± 7
D269A	90 ± 5	101 ± 11	87 ± 9	166 ± 5	188 ± 9	177 ± 6	180 ± 6	200 ± 9	155 ± 6	212 ± 11
R441A	95 ± 7	105 ± 11	127 ± 7	160 ± 7	174 ± 11	92 ± 5	181 ± 12	198 ± 6	150 ± 5	211 ± 12
R523A	94 ± 7	106 ± 5	72 ± 9	155 ± 11	181 ± 9	174 ± 11	169 ± 7	192 ± 6	152 ± 7	213 ± 11
D527A	93 ± 6	109 ± 7	129 ± 5	163 ± 7	178 ± 11	162 ± 9	178 ± 5	103 ± 7	155 ± 11	151 ± 11
E606A	97 ± 5	99 ± 7	124 ± 9	167 ± 11	187 ± 6	104 ± 7	171 ± 7	192 ± 9	166 ± 11	208 ± 7
K695A	97 ± 3	101 ± 6	124 ± 9	162 ± 7	176 ± 9	175 ± 6	177 ± 5	97 ± 6	164 ± 12	114 ± 12
IDP										
K250A	94 ± 12	105 ± 10	131 ± 7	165 ± 9	–	–	177 ± 9	202 ± 11	160 ± 5	208 ± 6
K261A	91 ± 11	103 ± 9	172 ± 12	–	–	–	194 ± 11	195 ± 5	214 ± 7	207 ± 5
E268A	88 ± 5	107 ± 11	168 ± 7	–	–	–	190 ± 11	190 ± 12	213 ± 7	210 ± 12
D269A	89 ± 11	106 ± 10	173 ± 8	–	–	–	195 ± 11	196 ± 12	215 ± 12	212 ± 11
R441A	93 ± 7	110 ± 12	187 ± 12	–	–	–	188 ± 7	191 ± 9	204 ± 11	218 ± 7
R523A	91 ± 11	111 ± 9	153 ± 7	–	–	–	197 ± 11	195 ± 12	212 ± 8	224 ± 11
D527A	95 ± 7	108 ± 11	189 ± 7	–	–	–	198 ± 7	113 ± 11	221 ± 11	164 ± 12
E606A	97 ± 5	107 ± 12	192 ± 11	–	–	–	187 ± 11	200 ± 6	220 ± 12	214 ± 7
K695A	96 ± 11	107 ± 7	134 ± 11	158 ± 9	–	–	191 ± 7	107 ± 12	207 ± 5	117 ± 9
PP_i										
K250A	97 ± 9	109 ± 7	124 ± 11	137 ± 9	–	201 ± 11	190 ± 11	204 ± 9	204 ± 12	207 ± 7
K261A	90 ± 7	112 ± 9	165 ± 7	–	–	192 ± 9	187 ± 9	211 ± 11	211 ± 7	209 ± 11
E268A	96 ± 5	104 ± 5	174 ± 9	–	–	197 ± 5	186 ± 5	190 ± 9	197 ± 5	218 ± 9
D269A	92 ± 11	101 ± 12	184 ± 11	–	–	187 ± 9	198 ± 7	198 ± 7	199 ± 7	219 ± 11
R441A	95 ± 12	114 ± 8	172 ± 9	–	–	87 ± 12	185 ± 7	196 ± 5	208 ± 11	215 ± 12
R523A	93 ± 11	102 ± 7	151 ± 11	–	–	187 ± 11	193 ± 11	195 ± 7	210 ± 7	225 ± 12
D527A	87 ± 12	98 ± 12	167 ± 9	–	–	182 ± 9	192 ± 12	105 ± 5	214 ± 12	142 ± 12
E606A	98 ± 5	99 ± 11	175 ± 9	–	–	98 ± 11	185 ± 12	203 ± 11	218 ± 9	214 ± 7
K695A	89 ± 7	104 ± 7	144 ± 9	167 ± 11	–	196 ± 7	197 ± 12	97 ± 12	211 ± 9	134 ± 11
P_i										
K250A	93 ± 6	101 ± 7	131 ± 5	158 ± 9	191 ± 11	176 ± 9	182 ± 5	202 ± 12	166 ± 11	218 ± 7
K261A	91 ± 7	105 ± 4	78 ± 10	154 ± 7	188 ± 9	170 ± 11	178 ± 12	204 ± 8	160 ± 11	209 ± 10
E268A	90 ± 10	106 ± 7	93 ± 14	160 ± 5	197 ± 9	171 ± 8	180 ± 11	205 ± 10	161 ± 7	224 ± 10
D269A	88 ± 7	108 ± 11	87 ± 7	163 ± 8	185 ± 5	168 ± 10	171 ± 11	187 ± 11	158 ± 9	217 ± 8
R441A	87 ± 8	110 ± 8	128 ± 10	151 ± 11	184 ± 10	95 ± 10	177 ± 11	197 ± 8	155 ± 11	213 ± 7
R523A	94 ± 7	104 ± 5	83 ± 11	155 ± 7	190 ± 10	170 ± 11	188 ± 11	203 ± 7	161 ± 10	207 ± 11
D527A	91 ± 9	107 ± 11	136 ± 14	169 ± 7	197 ± 11	161 ± 7	165 ± 5	104 ± 10	154 ± 9	114 ± 14
E606A	88 ± 9	110 ± 5	140 ± 9	174 ± 11	177 ± 9	101 ± 12	183 ± 5	197 ± 11	154 ± 7	203 ± 10
K695A	86 ± 7	105 ± 11	128 ± 5	163 ± 7	186 ± 12	174 ± 9	181 ± 12	87 ± 12	164 ± 7	118 ± 9

DISCUSSION

In previous reports, radiation inactivation revealed that the functional size of H^+-PPase was dimeric, followed by subsequent confirmation using size exclusion chromatography and x-ray crystallography (Fig. 2*D*) (2, 8, 9, 17). Using AFM, we have visualized here the image of a single molecule H^+-PPase in a lipid membrane. In addition, SMFS was utilized to unfold the H^+-PPase from the lipid bilayer. The fully stretched F-Ds extracted by AFM probe was selected for full extraction polypeptide of H^+-PPase out of the membrane. The gold-coated AFM probe was then employed to identify the tip-binding site at cysteine residues of the membrane-embedded H^+-PPase. With the fully stretched polypeptide and gold-coated AFM tip, the AFM tip-binding site might be referred to locate at the cysteine residues (Cys^{74} and Cys^{715}) of the N- or C-terminal loops (loop 1 or loop 15). The F-D analysis of C74S and C715S

TABLE 5
Locations of the force boundaries
Count lengths represent most probable peak positions (calculated in amino acids) obtained from Gaussian fits to the count length distributions. The dash indicates those not detectable on the AFM F-Ds.

Location (aa)	Force 1	Force 2	Force 3	Force 4	Force 5	Force 6	Force 7	Force 8
Control	123 ± 10	175 ± 12	259 ± 12	315 ± 8	374 ± 12	445 ± 11	478 ± 9	704 ± 10
IDP	124 ± 9	176 ± 13	281 ± 17	–	–	472 ± 15	–	699 ± 12
PP_i	127 ± 10	177 ± 9	283 ± 11	–	374 ± 13	476 ± 12	–	698 ± 12
P_i	123 ± 9	175 ± 12	260 ± 12	314 ± 13	374 ± 11	443 ± 11	479 ± 7	702 ± 12

variants indicated that Cys^{74} is the residue of the gold-coated AFM tip to H^+-PPase (Fig. 4*D*). Moreover, DTT was used to verify the tip-binding site, and the F-Ds of H^+-PPase were consequently altered at first force peak indicating the disulfide bond at Cys^{124}–Cys^{132} was conceivably reduced. Furthermore, the original peak 1 in wild type H^+-PPase was declined in C124S and C132S variants (Table 2). Therefore, the AFM probe was identified to attach the N-terminal loop (loop 1) at the Cys^{74} residue. Two explanations might elucidate this phenomenon. First, the N-terminal loop is the longest loop at the cytoplasm that provides a higher opportunity to interact with the AFM probe. Second, the N-terminal loop is a random coil structure with high flexibility that is hard to detect by x-ray crystallography (2). The higher flexibility of the loop promoted a better opportunity to interact with the AFM probe. Therefore, the gold-coated AFM probe was used to specifically anchor the N-terminal loop at Cys^{74}.

In the control state, the F-Ds of the H^+-PPase showed 10 force peaks contributed by several force boundaries along the transmembrane domains. These force boundaries might come from the protein-protein and/or protein-lipid interactions, such as salt bridges, hydrogen bonds, and hydrophobic interactions between TMs (21, 24, 34). The gold-coated AFM probe bound presumably to the Cys^{74} residue of H^+-PPase and extracted the polypeptide out of the membrane. The first energy barrier to unfold the H^+-PPase might come from the disulfide bond of Cys^{124}–Cys^{132} at loop 2 forming force peak 1 (Table 2). Furthermore, it is possible the Lys^{261} at TM5 formed a salt bridge network with TM6, TM12, and TM15, although Asp^{269} at TM6 linked to Arg^{523} at TM12, with both working together to contribute the force peak 3 (2). The F-D analysis revealed that K261A, E268A, D269A, and R523A variants yielded similar force strengths with WT H^+-PPase except for the force peak 3 (Table 4). The interaction force of peak 3 in K261A, E268A, D269A, and R523A variants was decreased to 64.1, 70.2, 66.4, and 54.9%, respectively, as compared with WT. In addition, the force strength of peak 6 for R441A and E606A variants was reduced to 52.9 and 59.7% of WT, respectively (Table 4). Therefore, the results further confirmed the salt bridges from the subunit-subunit interaction at the position of Arg^{441}–Glu^{606} and caused force peak 6. Moreover, the force strength of D527A and K695A variants declined to 50.7 and 47.8% of WT at force peak 8, and to 68.6 and 51.8% of WT at force peak 10 (Table 4). Thus, it was believed that the Glu^{527} on TM12 interacting with the Lys^{695} on TM15 probably generates the force peak 8 and 10 (Table 6). Furthermore, the hydrophobic interactions between two subunits are accountable to force peaks 7–10, respectively (Table 6). Besides the interaction forces, the secondary structure on loop 6 and 8 answered the force peaks 4 and 5, respectively, and these structures created the energy barriers when unfolding the H^+-PPase by AFM force spectroscopy (35). Notwithstanding, we cannot exclude the possibility that other residues might contribute the force boundaries upon modification of the H^+-PPase by AFM probe. Nevertheless, it is conceivable that these interaction forces or the structural barriers stabilize the H^+-PPase embedded in lipid bilayer and made up the force boundaries when the H^+-PPase was unfolded by AFM.

TABLE 6
Force boundaries and their relative interaction forces
The residues and domains involved in force boundaries of H^+-PPase were determined by AFM F-D.

Interaction force	Force peaks	Residues/domains
Disulfide bond	I	Cys^{124}–Cys^{132}
Salt bridge	III, VI, VIII, IX, X	Lys^{261}, Glu^{268}, Asp^{269}, Arg^{441}, Arg^{523}, Asp^{527}, Glu^{606}, Lys^{695}
Structure barrier	II, IV, V, VII	TM3–4, TM6–7, TM8–9, TM10–11
Hydrogen bond	VI, IX	Arg^{441}, Val^{568}, Val^{570}, Tyr^{587}, Arg^{609}
Hydrophobic interaction	VII, VIII, IX, X	TM10, -12, -13, -15, -16

In the presence of the substrate analog, IDP, the F-Ds were altered indicating IDP induced changes in transmembrane domain interactions. These results were consistent with previous reports that the substrate-binding sites were located at loop 5 between TM5 and TM6 (1, 23, 26). The binding of IDP tuned the conformational change of H^+-PPase to reduce the domain interaction of force peaks 5 and 6, respectively (Fig. 5*E*). In addition, the force peak 3 was diminished in the presence of IDP revealing the binding of IDP induced the conformational change with associated modification at the force boundaries of TM5 and -6. Further identification of the IDP binding altered the number of force peaks, and K250A and K695A variants were restored the force peaks 3 and 4 as the WT. However, the abolished force peaks 5 and 6 could not be recovered from the two variants in the presence of IDP (Table 4). In contrast to IDP, PP_i is the natural substrate of H^+-PPase that could be hydrolyzed thus releasing the force boundaries of TM5 and -6, whereas the IDP, an unhydrolyzable substrate analog, binds strongly with the H^+-PPase for consequent conformational changes of TM8 (force peak 5). Therefore, IDP might induce a state for H^+-PPase to accommodate the substrate analog without further hydrolysis. In the last step of PP_i hydrolysis, the product, P_i, was bound to the H^+-PPase before releasing (2, 17). The F-Ds of H^+-PPase in the presence of P_i indicated the similar pattern with the control state that contained 10 force peaks (Fig. 5*D*). These results showed that the P_i bound to H^+-PPase retained a conformation similar to the control state (2, 17).

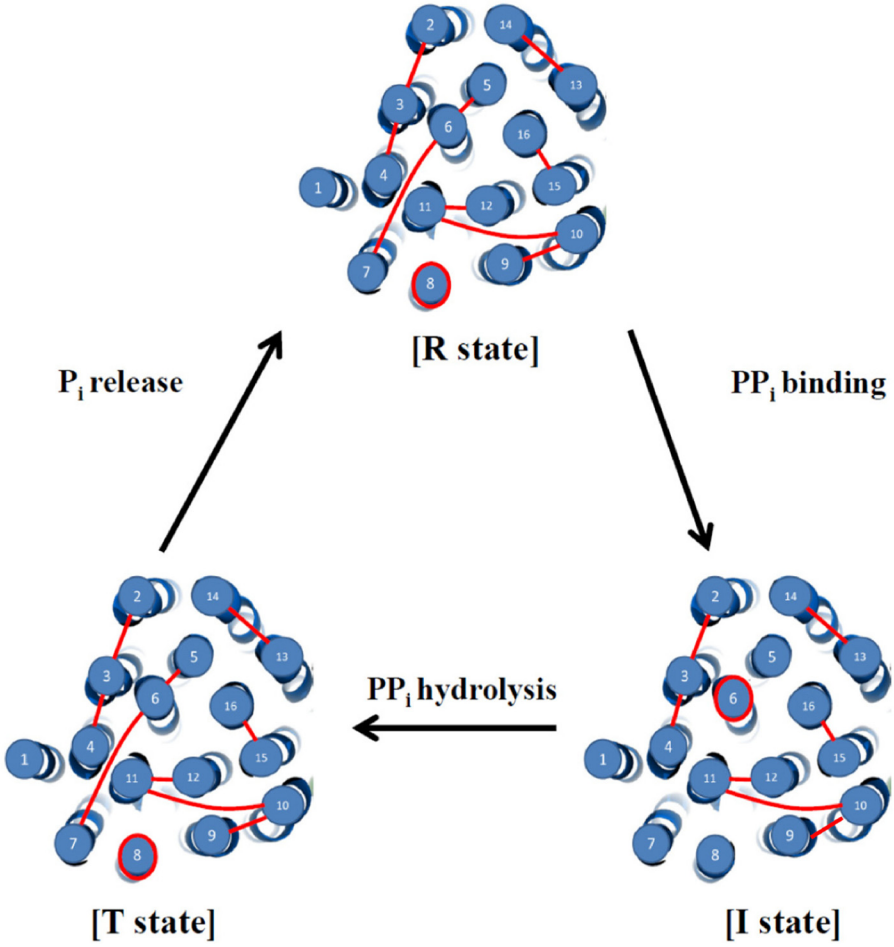

FIGURE 6. **Working model of the unfolding H^+-PPase by AFM probe.** The catalytic cycle contained resting state (*R state*), initiated state (*I state*), and transient state (*T state*). The AFM probe bound the N-terminal loop of H^+-PPase and extracted the membrane-embedded H^+-PPase out of the lipid bilayer. The *red lines* indicate the force boundaries as determined by smAFM. The dynamic movements of H^+-PPase as determined by AFM F-Ds at different conditions revealed the catalytic cycle for PP_i hydrolysis.

In summary, a working model was proposed to elucidate the domain interactions of H^+-PPase during the substrate hydrolysis according to the results mentioned above (Fig. 6). These conformational changes of H^+-PPase provided more precise PP_i hydrolysis mechanisms of H^+-PPase at different states (2, 17). The numbers of the force peaks were 10, 8, and 10 at R, I, and T states, respectively. This is the first study to identify the domain interactions of H^+-PPase by smAFM and suggests that the force boundaries from salt bridges, hydrogen bonds, hydrophobic interactions, and special structures provoked force boundaries in F-D curves. Moreover, dynamic movements of H^+-PPase induced by the substrate PP_i, substrate analog IDP, and product P_i were therefore identified by smAFM F-Ds. This study presents more detailed information on structure dynamics and the enzymatic mechanisms of H^+-PPase.

REFERENCES

1. Maeshima, M. (2000) Vacuolar H^+-pyrophosphatase. *Biochim. Biophys. Acta* **1465,** 37–51
2. Lin, S. M., Tsai, J. Y., Hsiao, C. D., Huang, Y. T., Chiu, C. L., Liu, M. H., Tung, J. Y., Liu, T. H., Pan, R. L., and Sun, Y. J. (2012) Crystal structure of a membrane-embedded H^+-translocating pyrophosphatase. *Nature* **484,** 399–403
3. McIntosh, M. T., Drozdowicz, Y. M., Laroiya, K., Rea, P. A., and Vaidya, A. B. (2001) Two classes of plant-like vacuolar-type H^+-pyrophosphatases in malaria parasites. *Mol. Biochem. Parasitol.* **114,** 183–195
4. Drozdowicz, Y. M., and Rea, P. A. (2001) Vacuolar H^+ pyrophosphatases: from the evolutionary backwaters into the mainstream. *Trends Plant Sci.* **6,** 206–211
5. Drozdowicz, Y. M., Kissinger, J. C., and Rea, P. A. (2000) AVP2, a sequence-divergent, K^+-insensitive H^+-translocating inorganic pyrophosphatase from *Arabidopsis*. *Plant Physiol.* **123,** 353–362
6. Belogurov, G. A., and Lahti, R. (2002) A lysine substitute for K^+-A460K mutation eliminates K^+ dependence in H^+-pyrophosphatase of *Carboxydothermus hydrogenoformans*. *J. Biol. Chem.* **277,** 49651–49654
7. Hsu, S. H., Hsiao, Y. Y., Liu, P. F., Lin, S. M., Luo, Y. Y., and Pan, R. L. (2009) Purification, characterization, and spectral analyses of histidine-tagged vacuolar H^+-pyrophosphatase expressed in yeast. *Bot. Stud.* **50,** 291–301
8. Tzeng, C. M., Yang, C. Y., Yang, S. J., Jiang, S. S., Kuo, S. Y., Hung, S. H., Ma, J. T., and Pan, R. L. (1996) Subunit structure of vacuolar proton-pyrophosphatase as determined by radiation inactivation. *Biochem. J.* **316,** 143–147
9. Sarafian, V., Potier, M., and Poole, R. J. (1992) Radiation-inactivation analysis of vacuolar H^+-ATPase and H^+-pyrophosphatase from *Beta vulgaris* L. Functional sizes for substrate hydrolysis and for H^+ transport. *Biochem. J.* **283,** 493–497
10. Liu, T. H., Hsu, S. H., Huang, Y. T., Lin, S. M., Huang, T. W., Chuang, T. H., Fan, S. K., Fu, C. C., Tseng, F. G., and Pan, R. L. (2009) The proximity between C termini of dimeric vacuolar H^+-pyrophosphatase determined using atomic force microscopy and a gold nanoparticle technique. *FEBS J.* **276,** 4381–4394
11. López-Marqués, R. L., Pérez-Castiñeira, J. R., Buch-Pedersen, M. J., Marco, S., Rigaud, J. L., Palmgren, M. G., and Serrano, A. (2005) Large-

scale purification of the proton pumping pyrophosphatase from *Thermotoga maritima*: a "Hot-Solve" method for isolation of recombinant thermophilic membrane proteins. *Biochim. Biophys. Acta* **1716,** 69–76
12. Pan, Y. J., Lee, C. H., Hsu, S. H., Huang, Y. T., Lee, C. H., Liu, T. H., Chen, Y. W., Lin, S. M., and Pan, R. L. (2011) The transmembrane domain 6 of vacuolar H^+-pyrophosphatase mediates protein targeting and proton transport. *Biochim. Biophys. Acta* **1807,** 59–67
13. Lee, C. H., Pan, Y. J., Huang, Y. T., Liu, T. H., Hsu, S. H., Lee, C. H., Chen, Y. W., Lin, S. M., Huang, L. K., and Pan, R. L. (2011) Identification of essential lysines involved in substrate binding of vacuolar H^+-pyrophosphatase. *J. Biol. Chem.* **286,** 11970–11976
14. Van, R. C., Pan, Y. J., Hsu, S. H., Huang, Y. T., Hsiao, Y. Y., and Pan, R. L. (2005) Role of transmembrane segment 5 of the plant vacuolar H^+-pyrophosphatase. *Biochim. Biophys. Acta* **1709,** 84–94
15. Lin, H. H., Pan, Y. J., Hsu, S. H., Van, R. C., Hsiao, Y. Y., Chen, J. H., and Pan, R. L. (2005) Deletion mutation analysis on C-terminal domain of plant vacuolar H^+-pyrophosphatase. *Arch. Biochem. Biophys.* **442,** 206–213
16. Hsiao, Y. Y., Van, R. C., Hung, S. H., Lin, H. H., and Pan, R. L. (2004) Roles of histidine residues in plant vacuolar H^+-pyrophosphatase. *Biochim. Biophys. Acta* **1608,** 190–199
17. Kellosalo, J., Kajander, T., Kogan, K., Pokharel, K., and Goldman, A. (2012) The structure and catalytic cycle of a sodium-pumping pyrophosphatase. *Science* **337,** 473–476
18. Lo, Y. Y., Hsu, S. H., Ko, Y. C., Hung, C. C., Chang, M. Y., Hsu, H. H., Pan, M. J., Chen, Y. W., Lee, C. H., Tseng, F. G., Sun, Y. J., Yang, C. W., and Pan, R. L. (2013) Essential calcium binding cluster of *Leptospira* LipL32 for inflammatory responses through the Toll-like receptor 2 pathway. *J. Biol. Chem.* **288,** 12335–12344
19. Hsu, S. H., Lo, Y. Y., Tung, J. Y., Ko, Y. C., Sun, Y. J., Hung, C. C., Yang, C. W., Tseng, F. G., Fu, C. C., and Pan, R. L. (2010) Leptospiral outer membrane lipoprotein LipL32 binding on toll-like receptor 2 of renal cells as determined with an atomic force microscope. *Biochemistry* **49,** 5408–5417
20. Frederix, P. L., Bosshart, P. D., and Engel, A. (2009) Atomic force microscopy of biological membranes. *Biophys. J.* **96,** 329–338
21. Hertadi, R., Gruswitz, F., Silver, L., Koide, A., Koide, S., Arakawa, H., and Ikai, A. (2003) Unfolding mechanics of multiple OspA substructures investigated with single molecule force spectroscopy. *J. Mol. Biol.* **333,** 993–1002
22. Kedrov, A., Janovjak, H., Sapra, K. T., and Müller, D. J. (2007) Deciphering molecular interactions of native membrane proteins by single-molecule force spectroscopy. *Annu. Rev. Biophys. Biomol. Struct.* **36,** 233–260
23. Müller, D. J., and Engel, A. (2007) Atomic force microscopy and spectroscopy of native membrane proteins. *Nat. Protoc.* **2,** 2191–2197
24. Kessler, M., and Gaub, H. E. (2006) Unfolding barriers in bacteriorhodopsin probed from the cytoplasmic and the extracellular side by AFM. *Structure* **14,** 521–527
25. Hsiao, Y. Y., Pan, Y. J., Hsu, S. H., Huang, Y. T., Liu, T. H., Lee, C. H., Lee, C. H., Liu, P. F., Chang, W. C., Wang, Y. K., Chien, L. F., and Pan, R. L. (2007) Functional roles of arginine residues in mung bean vacuolar H^+-pyrophosphatase. *Biochim. Biophys. Acta* **1767,** 965–973
26. Huang, Y. T., Liu, T. H., Chen, Y. W., Lee, C. H., Chen, H. H., Huang, T. W., Hsu, S. H., Lin, S. M., Pan, Y. J., Lee, C. H., Hsu, I. C., Tseng, F. G., Fu, C. C., and Pan, R. L. (2010) Distance variations between active sites of H^+-pyrophosphatase determined by fluorescence resonance energy transfer. *J. Biol. Chem.* **285,** 23655–23664
27. Bradford, M. M. (1976) A rapid and sensitive method for the quantitation of microgram quantities of protein utilizing the principle of protein-dye binding. *Anal. Biochem.* **72,** 248–254
28. Lévy, D., Mosser, G., Lambert, O., Moeck, G. S., Bald, D., and Rigaud, J. L. (1999) Two-dimensional crystallization on lipid layer: a successful approach for membrane proteins. *J. Struct. Biol.* **127,** 44–52
29. Butt, H.-J., and Jaschke, M. (1995) Calculation of thermal noise in atomic force microscopy. *Nanotechnology* **6,** 1–7
30. Mimura, H., Nakanishi, Y., Hirono, M., and Maeshima, M. (2004) Membrane topology of the H^+-pyrophosphatase of *Streptomyces coelicolor* determined by cysteine-scanning mutagenesis. *J. Biol. Chem.* **279,** 35106–35112
31. Sato, M. H., Kasahara, M., Ishii, N., Homareda, H., Matsui, H., and Yoshida, M. (1994) Purified vacuolar inorganic pyrophosphatase consisting of a 75-kDa polypeptide can pump H^+ into reconstituted proteoliposomes. *J. Biol. Chem.* **269,** 6725–6728
32. Britten, C. J., Zhen, R. G., Kim, E. J., and Rea, P. A. (1992) Reconstitution of transport function of vacuolar H^+-translocating inorganic pyrophosphatase. *J. Biol. Chem.* **267,** 21850–21855
33. Levy, D., Chami, M., and Rigaud, J. L. (2001) Two-dimensional crystallization of membrane proteins: the lipid layer strategy. *FEBS Lett.* **504,** 187–193
34. Janovjak, H., Kessler, M., Oesterhelt, D., Gaub, H., and Müller, D. J. (2003) Unfolding pathways of native bacteriorhodopsin depend on temperature. *EMBO J.* **22,** 5220–5229
35. Damaghi, M., Bippes, C., Köster, S., Yildiz, O., Mari, S. A., Kühlbrandt, W., and Muller, D. J. (2010) pH-dependent interactions guide the folding and gate the transmembrane pore of the beta-barrel membrane protein OmpG. *J. Mol. Biol.* **397,** 878–882